



Solid-state silicon anode with extremely high initial coulombic efficiency†

Cite this: DOI: 10.1039/d2ee04057c

Yonglin Huang,^a Bowen Shao,^a Yan Wang^{*b} and Fudong Han^{id} ^{*a}

Silicon is considered an important anode material for solid-state batteries (SSBs) because of its unique properties in addressing key challenges associated with Li metal anodes such as dendrite formation and morphological instability. Despite many exciting results from previous reports on solid-state Si anodes, the initial Coulombic efficiency (ICE), a critical parameter that characterizes the electrochemical reversibility for the first cycle and directly influences the energy density of the battery, has not been well considered. Here we study the electrochemical stability between Si and three representative solid electrolytes (SEs), including a typical sulfide (75Li₂S-25P₂S₅, LPS), an iodide-substituted sulfide (70(0.75Li₂S-0.25P₂S₅)-60LiI, LPSI), and a hydride-based SE (3LiBH₄-LiI, LBHI), to improve the ICE of solid-state Si anodes. Combining first-principles computations, electrochemical measurements, *ex situ* XPS characterizations, and mechanical measurements, we report that LBHI demonstrates superior electrochemical and chemical stability with Si anodes compared with sulfide-based SEs, enabling a high-performance solid-state Si anode with a record high ICE of 96.2% among all Si anodes reported to date. The excellent stability of LBHI with Si anode was also demonstrated in solid-state full cells with nickel-rich layered oxide cathodes. The research provides novel insights into developing high-performance Si anodes for practical applications.

Received 16th December 2022,
Accepted 20th February 2023

DOI: 10.1039/d2ee04057c

rsc.li/ees

Broader context

Due to several outstanding advantages, such as high capacity, low potential, low price, natural abundance, and environmental friendliness, silicon shows great potential as an alternative anode for next-generation batteries. Solidifying Si anodes with inorganic solid electrolytes has been reported as a promising direction for the development of high-performance Si anodes. However, the key challenge of low initial Coulombic efficiency has not been well considered for solid-state Si anode. Here, we study the (electro)chemical stability between various solid electrolytes and Si anode. Compared with commonly used sulfide-based solid electrolytes, theoretical and experimental characterizations demonstrate the excellent (electro)chemical stability of 3LiBH₄-LiI against Si. We also reveal the reaction mechanism between sulfide solid electrolytes and Si anode and discuss its implications on electrochemical performances. An extremely high initial Coulombic efficiency of 96.2% can be achieved for Si with 3LiBH₄-LiI solid electrolyte. The unique advantages of solid-state Si anodes with 3LiBH₄-LiI solid electrolyte are also demonstrated in solid-state full cells. This work provides new insights into the development of high-performance Si anodes.

Introduction

Solid-state batteries (SSBs) have attracted widespread attention due to their safety and potentially high energy density.¹ Anodes play an important role in the energy density of SSBs. Although the application of Li metal in SSBs can lead to a sharp increase

in the energy density, the utilization of Li metal with solid electrolytes (SEs) still faces key fundamental challenges including interfacial instability with SEs,²⁻⁴ Li dendrite formation during plating,⁵ and Li morphological instability during stripping.^{6,7} As a result, alternative anode materials including intercalation, alloying, and conversion-type electrodes are being explored for SSBs.⁸⁻¹⁰ Among all the anode materials, Si is considered one of the most promising alternatives to Li metal, because it exhibits a similarly high theoretical capacity (3579 mA h g⁻¹ based on Li₁₅Si₄) and relatively low electrode potential (0.4 V vs. Li⁺/Li).¹¹ While the cell-level energy density of SSBs made of Si anodes is expected to be lower than that of Li metal-based SSBs, the energy density at the pack and system levels can still be quite competitive in comparison with

^a Department of Mechanical, Aerospace and Nuclear Engineering, Rensselaer Polytechnic Institute, 110 8th Street, Troy, New York 12180, USA.
E-mail: hanf2@rpi.edu

^b Advanced Materials Lab, Samsung Advanced Institute of Technology-America, Samsung Semiconductor Inc., Cambridge 02138, MA, USA.
E-mail: eric.wangyan@samsung.com

† Electronic supplementary information (ESI) available. See DOI: <https://doi.org/10.1039/d2ee04057c>

conventional lithium-ion batteries (LIBs) by enabling the bipolar design and lowering the requirements for thermal management.¹² Besides, Si has several other advantages: low price, natural abundance, and environmental friendliness.¹³

Although Si has been explored as an anode material in conventional LIBs for several decades,^{14,15} its full-scale commercialization has proven difficult mainly due to side reactions between Si (and/or lithiated Si) and liquid electrolytes. These unwanted side reactions lead to fast capacity decay and limited calendar life of <20 months.^{16–18} The huge volume change (up to 300%) during lithiation also leads to pulverization that can further promote the degradation of Si anodes. Extensive research has been done in microstructure engineering,¹⁵ binder development,^{19–22} and electrolyte/additive optimization^{23,24} to address these challenges but the performance of Si anodes remains limited for practical applications. “Solidifying” Si anodes with inorganic SEs has been considered a promising approach to mitigate side reactions at the electrode/electrolyte interface because the solid electrolyte interphase (SEI) formation in SSBs is expected to be less dynamic than in LIBs, *i.e.*, SEI was “frozen” at the interface once it was formed. The non-flowable and non-infiltrative features of SEs can eliminate the need to re-form part of SEI on newly exposed electrode surfaces due to pulverization. While the large volume change of Si may seem to be a significant challenge for its use in the mechanically hard environment of SSBs, recent reports indicate that this may not be an issue in SSBs due to the excellent mechanical property of lithiated Si, *i.e.*, the lithiated Si can easily deform to ensure good interfacial contact with SEs,^{25,26} although detailed studies are still needed to (i) clarify whether these favourable deformations can occur under low stack pressure and (ii) understand the effect of stack pressure on the thermodynamics and kinetics of the lithiation/delithiation of Si.²⁷ The unique properties of SEs have enabled solid-state Si anodes with superior cycling performance compared with LIBs. While a variety of SEs has been used with Si anode, sulfide-based SEs are considered the most promising due to their excellent mechanical property and high ionic conductivity.^{28,29}

Even if the less dynamic SEI formation can mitigate the repeated growth of interphases and improve the cycle life of Si anodes, the utilization of SEs cannot prevent the Li inventory loss in the first cycle, characterized by the initial Coulombic efficiency (ICE), due to the irreversible electrochemical decomposition of SEs. It is commonly believed that for practical application ICEs of anodes should reach above 95% to minimize the amount of excessive cathode used to compensate for the Li loss.³⁰ Nevertheless, to the best of our knowledge, a solid-state Si anode that exhibits an ICE of >95% has not been reported. No Si anodes in the literature can deliver such high ICEs except for the pre-lithiated ones, regardless of the electrolyte state (liquid or solid). The low ICEs of Si anodes with sulfide SEs (78–86%) can be rationalized by the limited electrochemical stability windows of sulfide-based SEs (1.7 to 2.1 V *vs.* Li⁺/Li),³¹ *i.e.*, sulfide SEs will be reduced during Si lithiation and not all the decomposition reactions are reversible upon delithiation. Recent works have shown very promising results

using two-dimensional (2D) pure Si as the anode with sulfide-based SEs.^{11,26} The utilization of pure Si not only enables a long-cycling SSB due to the excellent mechanical property of lithiated Si but also leads to the formation of a 2D SEI that can cause less decomposition of SEs and reduce irreversible Li loss.²⁶ While high-performance 2D-type Si anodes certainly have important applications (*e.g.*, in thin film-type SSBs), utilizing 2D Si anodes for high-energy batteries with a high areal capacity can be quite challenging due to the insufficient electron and ion transports in pure Si. Given the limited electronic conductivity of pure Si (3×10^{-5} S cm⁻¹ for pressed micro Si),^{32,33} an electronic conductive additive is necessary for Si anode thicker than 1 μm to achieve high active material utilization.¹³ For practical application, the areal capacity of Si anodes should reach 4 mA h cm⁻² (corresponding to Si thickness >10 μm).¹³ Additional challenges for 2D Si include the mechanical instability of 2D SEI and the morphological instability of Si at the interface during long-term cycles. Therefore, a 3D anode composite consisting of Si, SE, and carbon to build a large number of three-phase contacts is necessary for the development of thick Si anodes. Unfortunately, the increase in the interfacial contacts in 3D anodes not only provides more electrochemical active sites for charge-transfer reactions of Si but also promotes the unwanted side reactions between SE and Si and between SE and carbon that can lead to low ICEs.

One promising approach to solve this well-known dilemma is to develop more stable electrolytes. SEs provide a unique advantage to address this challenge because different SEs can be used in the cathode and the anode depending on their electrochemical stability within certain voltages, while for conventional LIBs, the stability of liquid electrolytes with both the cathode and the anode will need to be considered due to the difficulties in separating two liquid electrolytes in a single cell. The development of a stable SE is also important to fully take advantage of this unique property of SEs to enable high Coulombic efficiencies (CEs) for the first cycle and subsequent cycles for high-energy-density and long-cycle-life Si anodes.

In this work, we aim to study the (electro)chemical stability of various SEs with Si anodes. Three representative SEs consisting of a typical sulfide SE (75Li₂S-25P₂S₅, LPS), a halide-substituted sulfide (70(0.75Li₂S-0.25P₂S₅)-60LiI, LPSI), and a hydride-based SE (3LiBH₄-LiI, LBHI) were studied for their application with Si anodes. LPSI was selected as one SE because of its better stability than LPS to enable graphite anodes,^{34–37} and LBHI was selected as another SE due to its excellent cathodic stability.³⁸ Combining first-principles computations, electrochemical and mechanical measurements, and *ex situ* characterizations, we reveal that side reactions between sulfide-based SEs (LPS and LPSI) and Si anodes are mainly associated with the interactions between Si and P, and show that LBHI demonstrates excellent electrochemical stability with Si anodes that can enable a record high ICE of 96.2%. The excellent performance of Si anodes with LBHI was also demonstrated in the cycling-stable solid-state full cell with the single-crystalline LiNi_{0.8}Co_{0.15}Al_{0.02}O₂ (NCA) cathode. Our work is one of the first studies to investigate the effect of SEs on the

electrochemistry of Si anodes and provides a viable approach by using electrochemically stable hydride-based SEs to address the challenges for developing high-performance 3D Si anodes for future SSBs.

Results and discussion

Computed (electro)chemical stability between Si and SEs

First-principles computation has proven to be a very powerful tool to predict the electrochemical and chemical stability of SEs and their interfaces with electrodes,^{31,39,40} and therefore we use this approach to understand the thermodynamic stability of SEs with Si anodes. Fig. 1 shows the computed electrochemical stability of Si with SEs in the voltage range of 0.0–1.5 V vs. Li⁺/Li. A more negative reaction energy means a higher thermodynamic driving force; thus, the reaction is more likely to occur. In practical application, it would be more desirable to have a high content of Si in the anode, so the reaction energy was calculated at different molar fractions of Si to fully understand the intrinsic stability between Si and SEs. Detailed information on predicted reaction processes including reaction voltages, reactant molar ratios, and reaction products is shown in Tables S1–S3 (ESI[†]). Data points at a molar fraction of 1.0 represent solely the reaction energy for the lithiation of Si and it does not depend on the compositions of SEs. The lithiation of Si starts to occur below 0.40 V vs. Li⁺/Li for all Si composites. The computed results predict the formation of Li₂₁Si₅ at voltages below 0.12 V vs. Li⁺/Li, while experimentally the composition of the most lithiated phase of Si is reported to be Li₁₅Si₄ possibly due to kinetics of lithiation,^{41–45} and therefore dashed lines are used to represent the reaction energy below 0.12 V vs. Li⁺/Li. The results at a molar fraction of 0.0 indicate the reaction energy for the electrochemical decomposition of SE itself. As shown in the left side of Fig. 1, at a molar fraction of 0.0, the reaction energy for the electrochemical decomposition of LPS, LPSI, and LBHI at 0 V vs. Li⁺/Li is 2.27, 1.93, and 0.30 eV per atom, respectively. The results are consistent with previous reports that iodide-substituted sulfide has slightly better cathodic stability than pure LPS and hydride-

based SEs demonstrate very good electrochemical stability at low voltages.^{34–37,46} Based on the voltages of the corresponding electrochemical reactions (Tables S1–S3, ESI[†]), the intrinsic reduction of LPS and LPSI already starts at voltages around 1.5 V vs. Li⁺/Li, while the reduction of LBHI itself cannot occur until 0.52 V vs. Li⁺/Li. Moreover, the decomposition of sulfide-based SEs at 1.7 V vs. Li⁺/Li has been observed experimentally.³¹ Li₂S, LiI, and P-containing materials, such as P, LiP₇, Li₃P₇, LiP, and Li₃P, are predicted to form under different voltages for sulfide-based SEs. On the other hand, no experimental results have been reported on the reduction of LBHI at low voltages. As the reduction of LBHI generates a highly stable, hydrogen-deficient, and complex polyhydro-*closo*-polyborate Li(BH)₆ with excellent redox stability,⁴⁷ it is likely that LBHI can be kinetically stabilized at low voltages. Even if slight decomposition occurs, the decomposition products LiH⁴⁶ and Li^{34–37} have been reported to be electronically insulating and electrochemically stable at 0 V vs. Li⁺/Li, so these insulating phases can help passivate interfaces.

Although the intrinsic electrochemical stability of the SE itself has been studied experimentally and theoretically in the past,^{31,39,40} the electrochemical stability between Si and SEs has never been studied to our knowledge. The reactions in the middle range (0.0 < molar ratio of Si < 1.0) of Fig. 1 show that the SEs possess distinct behaviors regarding the electrochemical stability with Si anodes. Multiple electrochemical reactions between Si and sulfide-based SEs (LPS and LPSI) with different Si/(Si + SE) ratios could occur starting at 1.5 V vs. Li⁺/Li, as reflected by the red color, while the reaction between Si and LBHI only occurs in a very small voltage range (0.38–0.36 V vs. Li⁺/Li, light blue color). The computation results in Table S3 (ESI[†]) show no electrochemical reactions occur between Si and LBHI at voltages higher than 0.38 V and lower than 0.36 V vs. Li⁺/Li, supporting the excellent electrochemical stability between Si and LBHI. The superior stability between Si and LBHI is also supported by much lower reaction energy (0.06–0.07 eV per atom), which can be easily suppressed by kinetics such as nucleation, growth, and solid-state diffusion, while the reaction energy for sulfide-based SEs is as high as 0.98 eV per atom. The calculated results shown in Tables S1 and S2 (ESI[†])

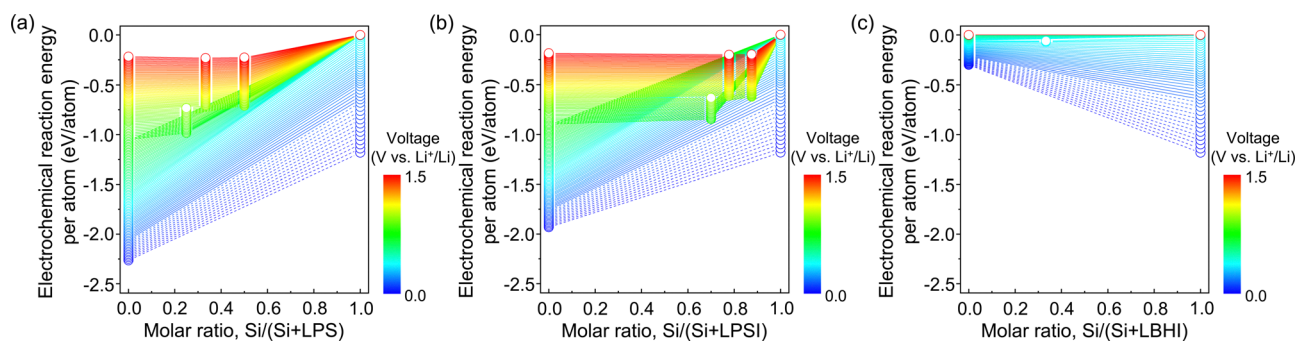


Fig. 1 Calculated electrochemical reaction energies between Si and (a) LPS, (b) LPSI, and (c) LBHI SEs. At a molar fraction of 0, the reaction energy for the electrochemical decomposition of SE itself is reflected; at a molar fraction of 1, only the reaction energy for Si lithiation is calculated. The dashed lines indicate the reaction energy below 0.12 V vs. Li⁺/Li, where Li₂₁Si₅ (at molar fraction of 1) is only available in calculations. The voltage interval used for calculations is 0.01 V vs. Li⁺/Li. The color bar represents a voltage range of 0.0–1.5 V vs. Li⁺/Li.

indicate the reactions between Si and sulfide-based SEs are mainly caused by the interactions between Si and P, forming SiP_2 , SiP , and Li_5SiP_3 which will then be further reduced to Li-Si and Li-P alloys at lower voltages. SiP_2 with the pyrite-type cubic structure (space group $Pa\bar{3}$, lattice parameter $a = 5.70 \text{ \AA}$) has been proposed as an electrode candidate for LIBs,^{48,49} although the exact electrode reaction mechanisms still need to be studied.^{48–51} While the reduction of P certainly increases the capacity for the first discharge process, the electrode potentials of these intermediate phases SiP_2 and SiP (1.5–0.97 V vs. Li^+/Li) and Li_5SiP_3 (0.96–0.76 V vs. Li^+/Li) are much higher than Si, leading to the increase of the anode potential and the decrease of ICEs due to the limited reversibility of these phases within the cut-off voltages of Si.

While three processes co-exist during the charge/discharge of anode composites: the lithiation and delithiation of Si, the electrochemical decomposition of SE itself at the interfaces with carbon, and electrochemical reactions between Si and SEs, their relative contributions are quite different for different SEs. For sulfide-based SEs, the reaction energy of the electrochemical decomposition of SEs is higher than that of the lithiation of Si. Considering that Li_{21}S_5 cannot be formed experimentally, the reaction energy of the electrochemical reactions between Si and sulfide-based SEs is also generally higher than that of the lithiation of Si to Li-Si with the highest possible lithium content experimentally, as shown in the magnified version of Fig. 1 (Fig. S1, ESI[†]). On the other hand, for LBHI, the reaction energy of the lithiation of Si is the highest, suggesting excellent electrochemical stability between LBHI and Si. In addition to

electrochemical stability, the chemical stability between Si/ $\text{Li}_{15}\text{Si}_4$ and SEs was also calculated based on the reaction energy (Fig. S2, ESI[†]) with more detailed reaction information in Tables S4 and S5 (ESI[†]). LBHI shows much better chemical stability with Si and $\text{Li}_{15}\text{Si}_4$ than sulfide-based SEs. The reaction energy between LBHI and Si is zero, indicative of no chemical reactions will occur, but the highest reaction energy between sulfide-based SEs and Si is $> 0.1 \text{ eV}$ per atom. For $\text{Li}_{15}\text{Si}_4$, the largest reaction energy with LBHI (0.06 eV per atom) is also much lower than that with sulfide-based SEs ($\sim 0.5 \text{ eV}$ per atom).

Electrochemical characteristics of Si anodes with different SEs

To validate the computed results of the electrochemical and chemical stability between Si and SEs, the electrochemical performance of Si anodes with different SEs was first evaluated in solid-state half cells with Li-In alloy as counter and reference electrodes at $210 \text{ mA g}_{\text{Si}}^{-1}$ at $60 \text{ }^\circ\text{C}$. Micro-sized Si was mixed with SEs and VGCF through ball milling with a mass ratio of 6 : 4 : 1. No apparent reactions between the components after ball milling can be observed from the XRD results (Fig. S3, ESI[†]) and the SEM/EDS results of the as-prepared anode composites show the similar distribution and morphology of the components (Fig. S4, ESI[†]). Fig. 2(a–c) show the charge/discharge profiles of Si anodes with different SEs. For sulfide-based SEs, as also reflected from the broad peak at around 0.6 V vs. Li^+/Li on the dQ/dV curves (Fig. S5(a and b), ESI[†]), a slope can be observed before entering the voltage plateau during the first discharge due to the electrochemical instability of sulfide-

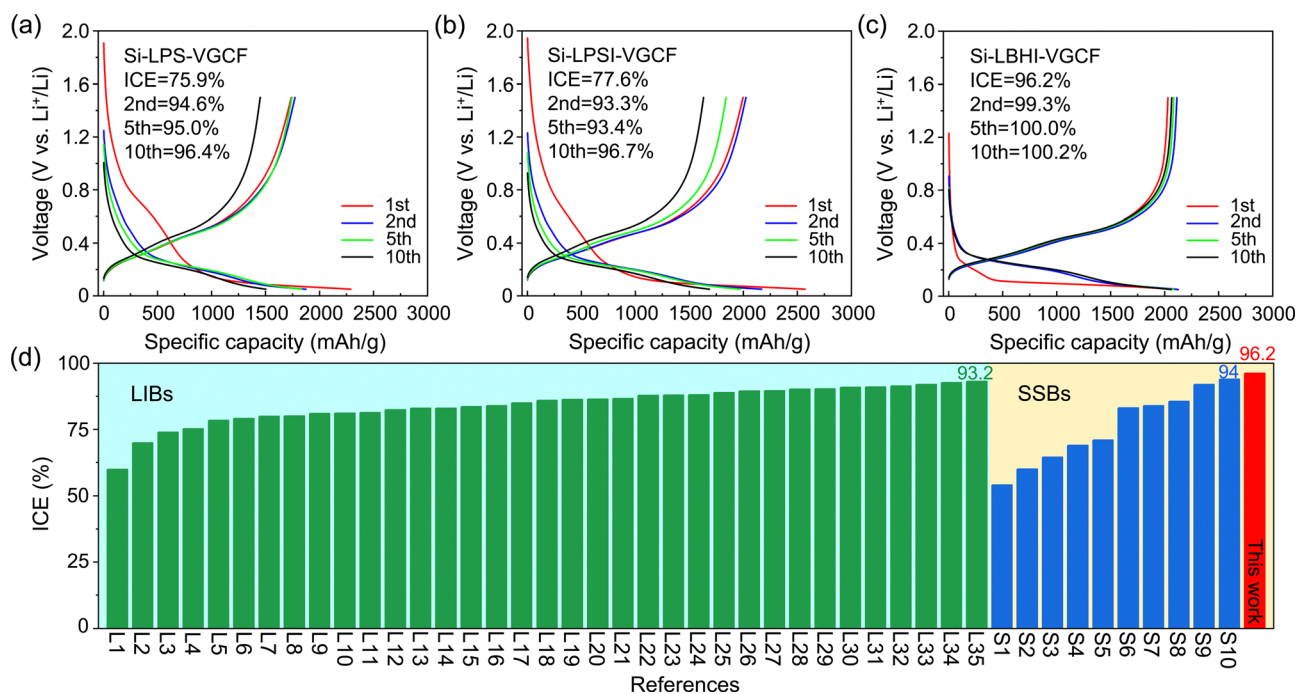


Fig. 2 (a–c) Charge/discharge curves of Si anodes using (a) LPS, (b) LPSI, and (c) LBHI SEs. The anode composites are denoted as Si-LPS-VGCF, Si-LPSI-VGCF, and Si-LBHI-VGCF based on the SE used. The current is $210 \text{ mA g}_{\text{Si}}^{-1}$ and the voltage range is 0.05–1.5 V vs. Li^+/Li (or -0.55 – 0.9 V vs. Li-In) at $60 \text{ }^\circ\text{C}$. The Si composites were prepared by ball milling micro-sized Si, SE, and VGCF in a mass ratio of 6 : 4 : 1. (d) Comparison of the ICEs of Si electrodes reported in LIBs and SSBs. The references for the listed ICEs are included in Table S6 (ESI[†]).

based SEs. More importantly, this redox behavior is not reversible during the subsequent charge process. For LBHI, the voltage quickly decreases to below 0.4 V vs. Li⁺/Li during the first discharge, followed by a small voltage slope between 0.29–0.17 V vs. Li⁺/Li and a very long voltage plateau until the cut-off voltage of 0.05 V vs. Li⁺/Li. The dQ/dV curve of the Si-LBHI-VGCF anode (Fig. S5(c), ESI[†]) also shows that no peaks can be observed before 0.29 V vs. Li⁺/Li and a prominent peak (0.1 V vs. Li⁺/Li) represents the long voltage plateau of the first discharge. The charge/discharge curves are similar to those of Si in liquid electrolytes,^{14,52,53} where the small slope between 0.29–0.17 V vs. Li⁺/Li is influenced by the irreversible lithiation of surficial silicon oxides.^{54,55} The voltage plateau indicates the lithiation of the crystalline Si in the first discharge. Since the cut-off voltage for discharge was not set to −0.6 V vs. Li–In (*i.e.*, 0 V vs. Li⁺/Li), Li–Si alloys formed in the first discharge would maintain an amorphous state without forming crystalline Li₁₅Si₄, as proved by Fig. S5(c) (ESI[†]), which is consistent with previous reports.^{41,56–58} The discharge curves from the second cycle show a different shape, which is highlighted by a voltage slope starting at about 0.36 V vs. Li⁺/Li, indicating the lithiation of amorphous Si. Moreover, all charge curves retain the sloping feature. The contribution of the electrochemical instability of SEs to the capacity for the first discharge process is supported by the large irreversible capacities that can be observed for LPS-VGCF and LPSI-VGCF electrodes (without Si) while the capacity for LBHI-VGCF is negligible (Fig. S6, ESI[†]). The distinct electrochemical behaviors also lead to sharp differences in the reversibility during the first cycle. From Fig. 2(a–c), the charge/discharge capacities for the first cycle are 1739/2289, 1997/2573, and 2030/2111 mA h g^{−1}, leading to an ICE of 75.9%, 77.6%, and 96.2% for Si-LPS-VGCF, Si-LPSI-VGCF, and Si-LBHI-VGCF, respectively. The slightly higher capacities and ICE of LPSI than LPS are mainly caused by the higher ionic conductivity (Fig. S7, ESI[†]) and cathodic stability of LPSI, respectively. Even though LBHI possesses the lowest ionic conductivity among the three SEs (Fig. S7, ESI[†]), it can enable the highest reversible capacity. In addition, Si-LBHI-VGCF exhibits very similar CEs and voltage profiles at lower contents of SE which is desired for increasing the energy density (Fig. S8, ESI[†]).

To the best of our knowledge, 96.2% is one of the highest ICE that has been reported for Si anodes regardless of the electrolytes used (liquid or solid), as shown in Fig. 2(d), highlighting the excellent stability of LBHI with Si. By optimizing the relative ratio of micro-sized Si, LBHI, and VGCF, the ICE can be further increased to 98.7% (Fig. S8(c), ESI[†]). The excellent electrochemical stability of LBHI can also be reflected by the CEs of the following cycles, *i.e.*, the CEs for Si anodes with sulfide-based SEs are still <97% after 10 cycles while the CE for Si-LBHI-VGCF reaches 99.7% in the 3rd cycle and 100% in the 5th cycle. By comparing the CEs of the first and second cycles of Si-LBHI-VGCF, we believe that the less than 4% capacity loss of the first cycle is induced primarily by the reduction of silicon oxides rather than the electrochemical instability of LBHI. In addition to low CEs, a quicker capacity decay can be observed for sulfide-based Si anodes, as supported by the cycling performance of Si anodes (Fig. S9, ESI[†]).

GITT and *ex situ* XPS study of reaction mechanisms of Si anodes with different SEs

To understand the effect of SEs on the electrochemistry of Si anodes for the following cycles, we measured the equilibrium potentials of Si anodes using the galvanostatic intermittent titration technique (GITT) for the second cycle (Fig. 3). The voltage profiles during GITT measurements (pulse time 0.5 h, relaxation time 3 h) were provided in Fig. S10 (ESI[†]). The measured potential after each titration can be considered as the thermodynamic equilibrium potential at each depth of charge/discharge without any kinetic effects. As shown in Fig. 3, Si anodes with sulfide-based SEs exhibit a much higher equilibrium potential than the theoretical potential of Si (0.4 V vs. Li⁺/Li) at a low normalized capacity. The result indicates that the electrochemical instability of sulfide-based SEs is partially reversible, affecting the potential and capacity during the following cycles. While it has been normally believed, especially in LIBs, that the effect of electrolyte decomposition on the electrochemistry of active material occurs mainly during the first cycle, the results here show that the effect of SEs on the redox behavior of Si can extend to the subsequent cycles. The increase in the potential of the Si anode will have a negative influence on the energy density of the cell when paired with a cathode. Moreover, the involvement of the partially reversible electrolyte instability in redox reactions of the anode also limits the utilization of Si due to the comprised electronic/ionic transport in the anode composite. The effect of SE instability on the electrode kinetics can be reflected from the similar apparent chemical diffusion coefficients of lithium for all three electrodes (Fig. S11, ESI[†]), despite that LBHI has a much lower ionic conductivity (Fig. S7, ESI[†]).

To further understand the reaction mechanism of Si anodes with different SEs, *ex situ* X-ray Photoelectron Spectroscopy (XPS) spectra of pristine, discharged, and one-cycled anodes

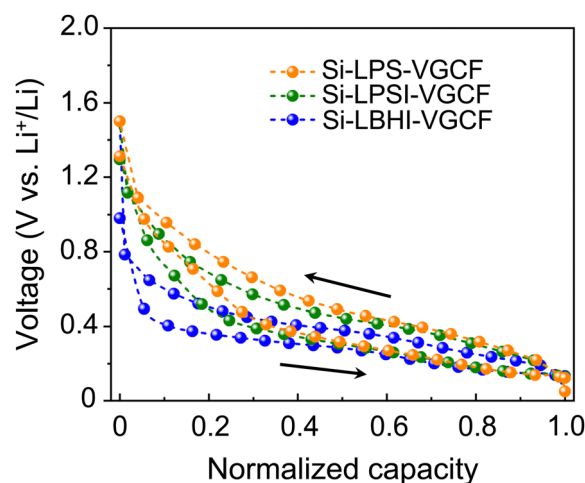


Fig. 3 GITT-derived equilibrium potential curves of Si anodes for the second cycle. The capacity of three anodes was normalized for ease of comparison. The mass ratio of micro-sized Si, SE, and VGCF is 4 : 6 : 1. The current value is 210 mA g_{Si}^{−1}. The cut-off voltage range is 0.05–1.5 V vs. Li⁺/Li.

were measured. The XPS spectra of pristine Si anode in Fig. 4(a), (c), and (e) show two peaks: one major peak at ~ 99.8 eV for Si and one shoulder peak at ~ 101.6 eV corresponding to the Si–O species on the surface. Comparing the binding energy of the shoulder peak with SiO_2 ^{59,60} and SiO ,^{61,62} the oxidation state of Si in the surface oxide is close to +2. The existence of Si–O species is also widely reported in the literatures.^{26,32} After discharging to 0.05 V vs. Li^+/Li , only one peak corresponding to the formation of Li–Si alloy can be observed at a lower binding energy of ~ 99.0 eV for all three anodes (Fig. 4(a), (c), and (e)). The results suggest the surface oxide layer on Si will be reduced to Li–Si alloy, and this reduction of the oxide layer is also consistent with the small slope between 0.29–0.17 V vs. Li^+/Li observed during the first discharge of Si-LBHI-VGCF anode (Fig. 2(c)). After charging to 1.5 V vs. Li^+/Li , the main peak shifts to a higher binding energy (~ 99.8 eV), corresponding to the oxidization of Li–Si alloy back to Si for all three anodes. Nevertheless, another small peak at a high binding energy of ~ 102.0 eV appears for Si anodes with sulfide-based SEs (Fig. 4(a) and (c)) but not for Si-LBHI-VGCF (Fig. 4(e)). This binding energy is higher than that of the Si–O species on the Si surface (~ 101.6 eV) but is lower than that of SiO_2 (~ 103.5 eV). It should be noted that the binding energy of Si will increase to a higher value when the oxidation state of Si increases and for Si with the same oxidization state, the binding energy increases as the electronegativity of the anions increases. The binding energy (~ 102.0 eV) higher than that of the Si–O species on the surface but lower than that of SiO_2 can exclude the possibility of assigning the small peak to Li–Si–O because the reduction of the surface Si–O species to Li–Si–O would lead to a shift to the lower binding energy.^{26,32} The computed results in Fig. 2(a and b) show the formation of SiP_2 , SiP , and Li_5SiP_3 compounds during the lithiation and delithiation of Si anodes with LPS and LPSI SEs. Due to the lower electronegativity of P (2.19) than O (3.44), at the same oxidation state of +4, the Si in Si–P will show a lower binding energy than SiO_2 . Therefore, we assign the side peak at ~ 102.0 eV to the formation of Si–P or Li–Si–P phases due to the electrochemical reactions between Si and sulfide-based SEs.

The electrochemical instability of sulfide-based SEs during charge/discharge can also be observed from the reduction and oxidation of P shown in the P 2p spectra (Fig. 4(b) and (d)), while no apparent change can be observed for LBHI after discharge and charge based on the XPS spectra of B 1s (Fig. 4(f)). B–O species detected from the B 1s spectra of LBHI are caused by the oxidation of LBHI during the sample transfer process. The reduction and oxidation of Si and P in the sulfide-based SEs are also expected to remain in the subsequent cycles, leading to an increase in the equilibrium potential, especially at a small normalized capacity (Fig. 3). The absence of PS_4^{3-} signals after discharge (Fig. 4(b) and (d)) can be explained by the reduction of the entire surfaces of LPS and LPSI particles, considering that XPS only analyzes substances within 5 nm of the surface, and VGCF will accelerate this reduction process. Overall, the XPS results demonstrate the much better electrochemical stability of LBHI than sulfide-based SEs with Si

anodes. The XPS results are also supported by the XRD results (Fig. S12, ESI[†]) of the anodes after the first discharge and after the first cycle where the formation of Li_2S and other crystalline phases can be observed for Si-LPS-VGCF (Fig. S12(a), ESI[†]) and Si-LPSI-VGCF (Fig. S12(b), ESI[†]) due to the decomposition of the sulfide-based SEs and no new phases can be observed in the Si-LBHI-VGCF anode (Fig. S12(c), ESI[†]). Both the XPS and XRD results agree very well with the computational and electrochemical results (Fig. 1 and 2).

Electrochemical performance of Si||NCA full cells

Si anodes with different SEs were paired with single-crystalline NCA cathodes to make solid-state full cells to validate the excellent electrochemical stability of LBHI for Si anodes. LPSCl was used as the SE in the NCA cathode. A bilayer SE was used to make the full cell with LPSCl near the cathode and LPS, LPSI, or LBHI near the anode depending on the SE used in the Si composite. As mentioned above, the non-flowable and non-mixing features of SEs enable the utilization of different SEs in each electrode based on their distinct electrochemical stability. The negative to positive capacity ratio (NP ratio) is set at 2.74 based on the theoretical capacity of Si (3579 mA h g^{-1}) and NCA (180 mA h g^{-1}). It should be noted that a high NP ratio poses a greater challenge for cell balancing if the ICE of the anode is low. Fig. 5(a–c) show the charge/discharge curves of the full cells. Due to the electrochemical instability of sulfide-based SEs in Si anodes, a large sloping plateau from about 2.5 to 3.5 V vs. Li^+/Li can be observed in Fig. 5(a and b) during the first charge. This low-voltage slope is not present in the Si anode with LBHI SE (Fig. 5(c)). Besides the passivating interphases formed by LPSCl oxidation at the cathode side,⁶³ the large capacity of this low-voltage slope also leads to a large irreversible capacity. The first-cycle charge/discharge capacities are 190.8/127.4, 198.9/136.9, and 203/152 mA h g^{-1} , leading to an ICE of 66.8%, 68.8%, and 74.7% for the full cells with Si-LPS-VGCF, Si-LPSI-VGCF, and Si-LBHI-VGCF anodes, respectively. Although the CE of the homemade NCA cathode still needs to be optimized, the results clearly show that utilization of LBHI can largely increase the reversible capacity and ICE for the full cells. The excellent electrochemical stability of LBHI also leads to a quick increase in the CE for the following cycles and the average CE of Si-LBHI-VGCF anode (99.34%) is much higher than that of sulfide-based Si anodes (98.56% for Si-LPS-VGCF and 98.70% for Si-LPSI-VGCF). Moreover, the voltage hysteresis in Fig. 5(a and b) becomes much larger with cycling. These overall lead to an improved cycling performance (Fig. 5(d)) for the full cell with Si-LBHI-VGCF anode. The excellent performances of the full cell with Si-LBHI-VGCF anode can also be achieved when the areal capacity of the cathode increases to 3 and 4 mA h cm^{-2} (Fig. S13, ESI[†]).

It should be noted that the cycling performance of Si||NCA full cells (Fig. 5(d)) is overall better than that of Si||Li–In half cells (Fig. S9, ESI[†]). In Si||Li–In half cells, the capacity of Li–In is overly excessive and in Si||NCA full cells, the capacity of Si is excessive to fully utilize the NCA cathode. Due to the large difference in Li inventory (*i.e.*, “infinite” Li inventory in the half

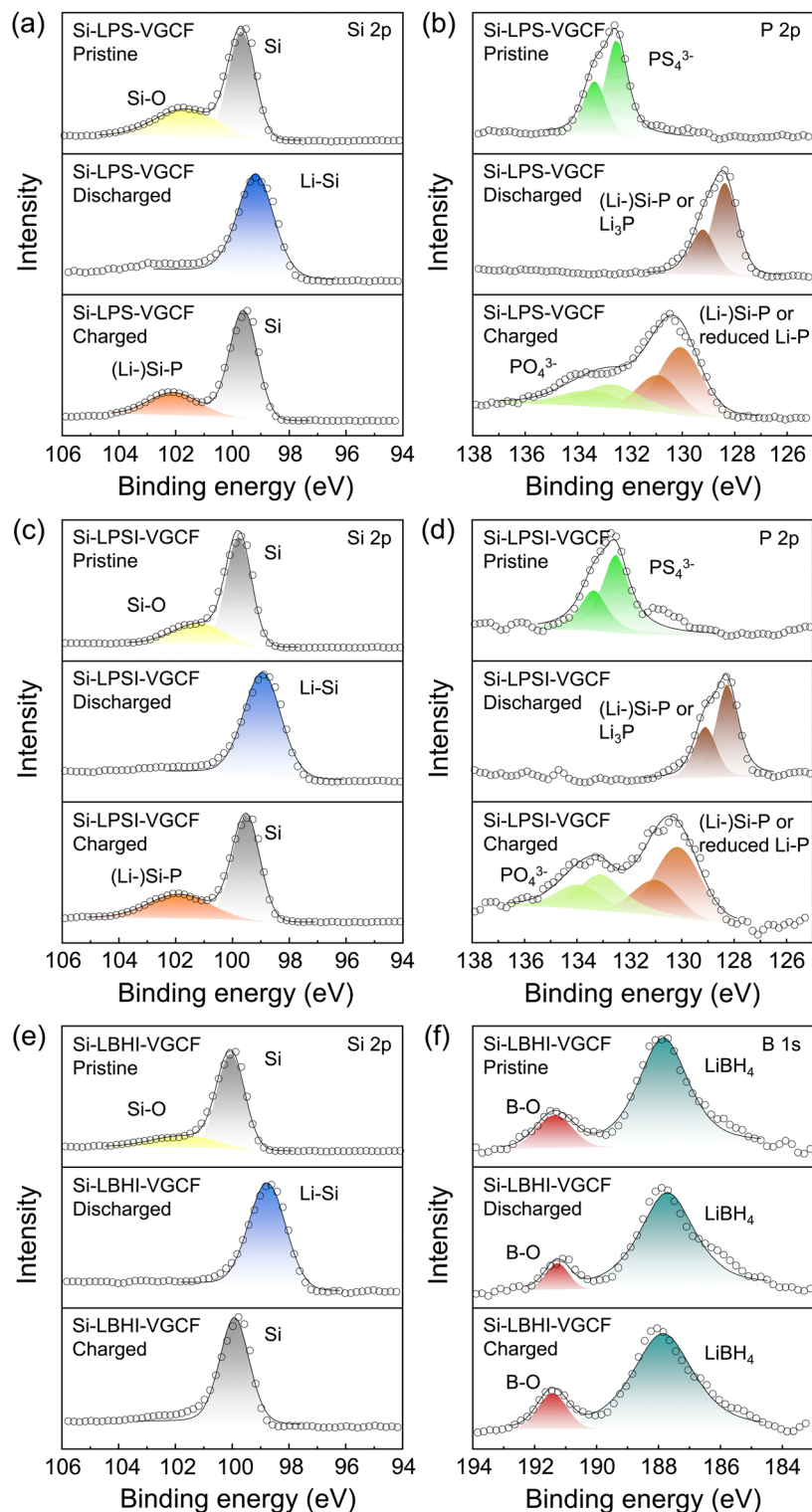


Fig. 4 *Ex situ* XPS spectra of (a) Si 2p and (b) P 2p from Si-LPS-VGCF, (c) Si 2p and (d) P 2p from Si-LPSI-VGCF, and (e) Si 2p and (f) B 1s from Si-LBHI-VGCF in the pristine state (top), after discharge (middle), and after one cycle (bottom). The mass ratio of micro-sized Si, SE, and VGCF is 4 : 6 : 1.

cells and limited Li inventory in the full cells), the degree of utilization of Si in the full cells is much lower than that in the half cells, and therefore the Si anodes in the full cells should

show better cycling stability than that in the half cells. The larger volume change of an alloying-type Li-In than an intercalation-type NCA also contributes to the improved cycling

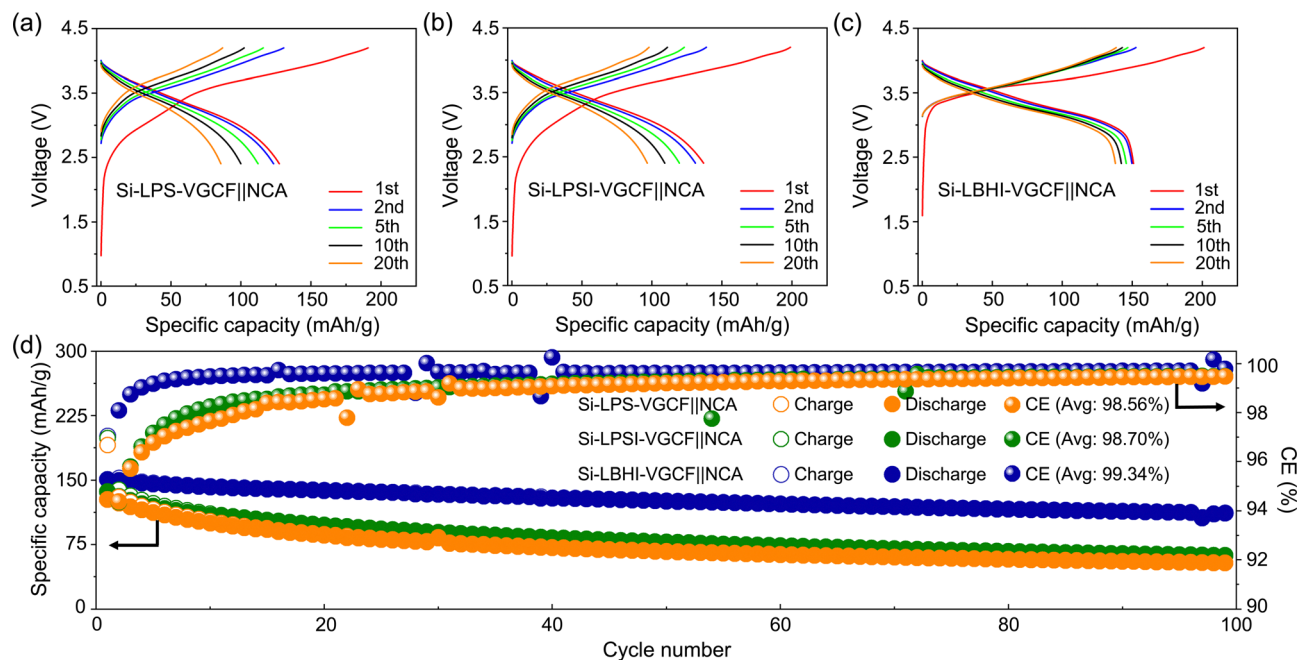


Fig. 5 Electrochemical performance of solid-state Si||NCA full cells. Charge/discharge profiles of solid-state Si||NCA full cells with (a) Si-LPS-VGCF, (b) Si-LPSI-VGCF, and (c) Si-LBHI-VGCF anodes. (d) Cycling performance and CEs of Si||NCA full cells with different anodes. The mass ratio of micro-sized Si, SE, and VGCF is 6 : 4 : 1. The cells were tested at 0.5C (= 0.785 mA) within a voltage range of 2.4–4.2 V at 60 °C. The areal capacity of cathode active materials is 2 mA h cm⁻².

performance of the full cells. A larger impedance rise can also be observed in the half cells than in the full cells (Fig. S14, ESI[†]).

Pressure evolution during charge/discharge of Si||NCA full cells

While significant improvements in the ICE, average CE, and cycling performance of the full cells can be achieved with Si-LBHI-VGCF anodes, capacity decay can still be observed for the first 100 cycles. Given the excellent chemical and electrochemical stability between LBHI and Si, we believe the capacity decay is heavily related to the large stress/strain generated during charge and discharge. Fig. 6 compares the pressure change of the full cells with the three Si anodes. Solid-state Si||NCA full cells were tested at a stack pressure of 70 MPa, and the deviation of the pressure from 70 MPa is shown in Fig. 6(a–c). The pressure of the cells increases during charge and decreases during discharge, suggesting that the pressure evolution is mainly dominated by the lithiation/delithiation of Si anodes based on the much smaller volume change of the cathode compared with the anode. This is also the reason why we studied the mechanics of solid-state Si anodes in Si||NCA full cells instead of Si||Li-In half cells because the pressure evolution of a full cell is dominated by the Si anode. Compared with the full cells with sulfide-based Si anodes, the cell with Si-LBHI-VGCF exhibits the largest pressure change during charge and discharge, although the discharge capacity is similar. Since the lithiation/delithiation of Si has a much larger volume change than the reduction and oxidation of SEs (Tables S7–S9, ESI[†]), the volume change of sulfide-based SEs (Tables S7 and S8, ESI[†]) due to electrochemical instability

would alleviate the cell-level pressure change, and the largest pressure change for Si-LBHI-VGCF anode means that the anode capacity is mainly provided by the lithiation/delithiation of Si. This is also supported by a more quantitative comparison of the normalized pressure per capacity (Fig. 6(d)), *i.e.*, Si-LBHI-VGCF anode demonstrates a higher stress/capacity ratio because it has a higher partial molar volume of Li (almost only contributed by Si) than the redox of sulfide-based SEs. The mechanical measurement confirms that the utilization of LBHI can lead to higher utilization of Si in the anodes.

To study the effect of the stack pressure on the performance of Si||NCA full cells, we evaluated the electrochemical performances of Si-LBHI-VGCF||NCA full cells at lower stack pressures (Fig. S15, ESI[†]). It can be observed that the capacity decreases as the stack pressure decreases. A quick capacity decay can also be observed from the cell tested under 10 MPa. The results call for a further detailed study of the mechanisms of capacity degradation under low stack pressures for practical applications. The evolution of cell impedance when cycling at different stack pressures (Fig. S16, ESI[†]) suggests that at 10 MPa the pressure is insufficient to maintain the interfacial contact between the electrode and electrolyte, while at 70 MPa the large strain/stress due to the volume change of the electrode can lead to degradations in the SE itself such as cracking, causing increases in the resistances of the SE. Nonetheless, the almost constant interfacial resistances when the cell is tested under 70 MPa suggest no apparent (electro)chemical instabilities between the electrode and electrolyte, supporting the excellent stability of LBHI against Si anodes. The stack pressure-dependent degradation mechanism also indicates that future work should be

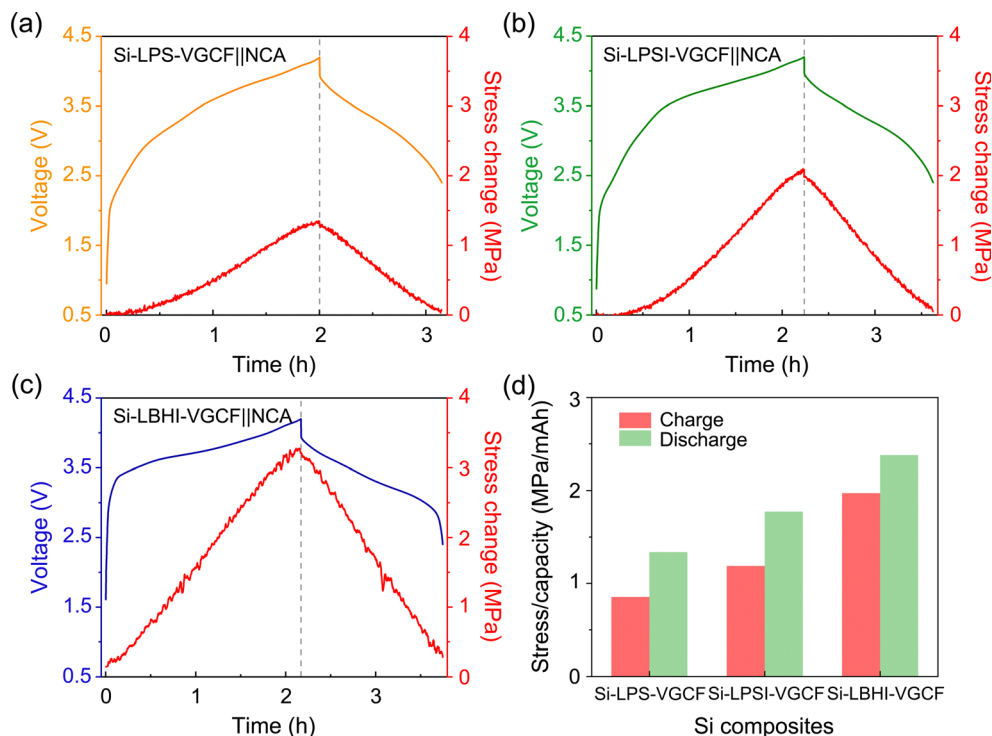


Fig. 6 Pressure change during the first charge and discharge of Si||NCA full cells with (a) Si-LPS-VGCF, (b) Si-LPSI-VGCF, and (c) Si-LBHI-VGCF anodes. (d) Stress change is normalized by the corresponding capacity of the full cells shown in (a), (b), and (c). These full cells were prepared and tested at the same conditions as the full cells shown in Fig. 5.

focused on improving interfacial contact between the electrode and SE at low stack pressure, *e.g.*, by designing a 3D host for the Si anode.

To further study the effect of mechanics on the electrochemical performance of solid-state Si anodes under stack pressure, we did a preliminary compression measurement on the cold-pressed SEs (Fig. S17, ESI[†]). The results show that the trend of elastic modulus is LPS > LPSI > LBHI. It has been reported that the slightly lower elastic modulus of LPSI than LPS helps to improve the cycling performance of solid-state Si anodes,²⁵ and therefore the improvement in the cycling performance of Si-LBHI-VGCF is not only caused by the minimal decomposition of LBHI but also related to the excellent mechanical property of LBHI. Nevertheless, simply replacing sulfide SEs with LBHI seems to be insufficient to address the capacity degradations of the micro-sized Si in SSBs. We suspect that one of the reasons for the capacity degradation of the Si-LBHI-VGCF anode is SE cracking. The ultimate compression strength of LBHI (81 MPa) is measured to be much lower than that of LPSI (119 MPa) and LPS (243 MPa). During the compression measurement, we also observe brittle fracture of LBHI, while sulfide-based SEs are more ductile. Under a high stack pressure, due to the reaction heterogeneity, local stress in the Si-LBHI-VGCF can easily exceed the ultimate compression strength of LBHI, leading to fractures and affecting the ionic percolation in the anode composite. We believe that utilizing LBHI with Si anode at lower stack pressure may improve the cycling performance, but challenges remain to maintain good

interfacial contact between the SE and Si during long-term cycles. Introducing polymeric binder that is chemically and electrochemically stable with both SE and Si is important. Another direction to improve the cycling performance of Si-LBHI-VGCF anode is engineering the microstructure, for example, using nanosized Si, to achieve a more uniform reaction and stress/strain distribution in the anode composite. The excellent electrochemical and chemical stability of LBHI is a very important advantage for enabling nanosized Si because the increased surface area will lead to even stronger side reactions with sulfide-based SEs. Our preliminary data (Fig. S18, ESI[†]) shows dramatic improvements in the cycling performance of Si-LBHI-VGCF after using nanosized Si as the active material in Si||Li-In half cell.

Moreover, VGCF is essential for Si composites by providing the electronic conduction pathway and additional volume to accommodate the strain/stress generated during charge and discharge. Solid-state Si anodes without VGCF such as Si-LPS (Fig. S19(a), ESI[†]) and Si-LPSI (Fig. S19(b), ESI[†]) have very low ICE (<26%) in the first cycle. Introducing VGCF improves the first discharge capacity as well as the ICE for Si-LPS-VGCF (2660 mA h g⁻¹, 54.2%, Fig. S19(d), ESI[†]) and Si-LPSI-VGCF (2910 mA h g⁻¹, 70.1%, Fig. S19(e), ESI[†]). The slight improvement in the first discharge capacity and ICE of Si-LBHI-VGCF (2170 mA h g⁻¹, 97.7%, Fig. S19(f), ESI[†]) is also attributed to VGCF (Si-LBHI: 2099 mA h g⁻¹, 92.0%, Fig. S19(c), ESI[†]). Fig. S19(f) (ESI[†]) exhibits voltage profiles similar to Fig. 2(c), and the improved first discharge capacities in Fig. S19(d) and (e) (ESI[†]) are caused by the higher proportion of SEs in sulfide-based composites.

It should also be noted that the synthesis and processing of hydride-based SEs are quite similar to typical sulfide-based SEs. Hydride-based SEs can be synthesized by ball-milling and solid-state synthesis methods, and cold-pressing at room temperature is sufficient to achieve a high ionic conductivity for typical hydride-based SEs for their integration into SSBs. The excellent solubility of hydrides in some solvents such as tetrahydrofuran (THF)^{64,65} and their low melting points⁶⁶ also provide opportunities for liquid (or molten) phase approaches to fabricate thin electrolyte films and electrode composites.

Conclusions

In summary, using a combined computational and experimental approach, we systemically investigated the chemical and electrochemical stability between Si and different SEs. Apparent electrochemical decomposition of sulfide-based SEs, LPS and LPSI, can be observed during the charge/discharge of Si anodes. The decomposition of SEs not only leads to a limited ICE (75.9% for LPS and 77.6% for LPSI) but also increases the electrode potential for subsequent cycles. The results from computation, GITT, and *ex situ* XPS have confirmed the electrochemical reactions between Si and P contained in sulfide-based SEs. On the other hand, no apparent electrochemical decomposition of LBHI can be observed from the Si anode with LBHI SE. The excellent electrochemical and chemical stability of LBHI leads to a Si anode with one of the highest ICE of 96.2% reported to date, regardless of the electrolyte used (liquid or solid). The electrochemical performance of Si-LBHI-VGCF anodes is also demonstrated in solid-state full cells. Si||NCA full cell using LBHI delivers a high discharge capacity of 152 mA h g⁻¹ at 0.5C with better cycling stability than LPSI and LPS full cells. Finally, based on the mechanical measurements, several approaches to mitigating the mechanical degradations are proposed to further improve the cycling performance of LBHI-based Si anodes. Our research provides novel insights for the future development of Si anodes for SSBs.

Experimental

Material synthesis

LPS, LPSI, and LBHI were prepared by solid-state synthesis. For the synthesis of LPS, Li₂S and P₂S₅ powders were weighed in the molar ratio of 3:1. The reactants were ball-milled at 510 rpm for 40 hours with a ball-to-material ratio of 30:1. For the synthesis of LPSI, Li₂S, P₂S₅, and LiI powders were weighed in the molar ratio of 21:7:12. The reactants were ball-milled at 500 rpm for 55 hours with a ball-to-material ratio of 30:1. The ionic conductivity of LPS and LPSI is about 0.5 and 1.2 mS cm⁻¹, respectively. The ball-milling processes were performed in ZrO₂ jars. For the synthesis of LBHI, LiBH₄ and LiI powders were weighed in the molar ratio of 3:1. The reactants were ball-milled at 400 rpm for 60 hours with a ball-to-material ratio of 50:1. The ionic conductivity of LBHI

is about 0.1 mS cm⁻¹ (Fig. S7, ESI†). The ball-milling process was performed in a tungsten carbide jar.

The micro-sized Si powders (1–5 μm, ≥99.9%, Alfa Aesar) were ball milled with SEs and vapor-grown carbon fiber (VGCF) in stainless-steel jars at 350 rpm for 5 hours. Li_{0.5}In composite electrodes (Li–In) were prepared by mixing the stoichiometric amounts of stabilized Li metal powders (FMC) and indium powders (99.99%, Sigma Aldrich) for 30 minutes, Li₆PS₅Cl (LPSCl, NEI Corporation) was then added to the metal powder mixture and mixed for another 15 minutes. The weight ratio of the metal powder mixture to LPSCl was 4:1. NCA cathodes were prepared by a solid-state reaction method following a previous publication.⁶⁷ The mass ratio of NCA, LPSCl, and VGCF is 65:33:2.

Material characterization

SEs and Si composite anodes were characterized by X-ray diffraction (XRD) with PANalytical X'Pert Diffractometer using a copper irradiation source (Cu Kα = 0.15406 nm). The morphology of Si composite anodes was analyzed by Zeiss Supra 55 field emission scanning electron microscope (FESEM) with a Schottky thermal field emission source. The element distribution of Si composites was mapped out by Energy Dispersive Spectrometry (EDS) equipped on FESEM. The *ex situ* surface chemistry of Si composite anodes was provided by X-ray Photoelectron Spectroscopy (XPS). The integrated ion sputtering can continuously remove the surface. The spectral resolution is <0.5 eV. The XPS signals are obtained from regions within about 5 nm of the surface. The XPS system is maintained under ultra-high vacuum conditions (~10⁻¹⁰ Torr).

First-principles computations

The calculations of the chemical and electrochemical reactivity of SEs with Si electrodes used the relevant energies of all relevant chemistries calculated by density functional theory in the Materials Project (<https://materialsproject.org>) and followed the methodology developed in the earlier works.^{4,46} For chemical reactivity calculations, we assumed the reaction between two solids (SE and Si electrode) at their interface may consume an arbitrary amount of each phase, and the reaction energy was determined by considering the mixing ratio that yielded the largest reaction driving force for the reaction energy calculations. For electrochemical reactivity under an applied voltage, the reactions were predicted by evaluating the grand potential under open-system conditions for lithium. In these calculations, the energies of materials that are not crystalline (*e.g.*, LPSI and LPS) were placed exactly on the convex hull of the computed phase diagram, assuming that they were stable on the convex hull and ignoring the small phase stability energies as compared to the large chemical and electrochemical reaction energies.

Electrochemical measurement

The Si||Li–In half cells were prepared by sandwiching two layers of SEs between electrodes. 80 mg LPSCl was firstly cold-pressed in the PEEK tube with a 10 mm diameter at

50 MPa. Then 20 mg LPS, 20 mg LPSI, or 10 mg LBHI were put and pressed on one side of the compacted LPSCl, followed by the addition of Si composites (mass ratio 6:4:1, 2.0 mg; 6:3:1, 1.8 mg; and 6:2:1, 1.6 mg) with the same SE. 200 mg Li-In composite was added to the other side of the LPSCl. Finally, the whole structure was pressed at 250 MPa to make a half cell. The electrochemical performance of half cells was tested within a voltage range of -0.55 – 0.9 V vs. Li-In by using the Arbin BT 2000 Battery Tester. The current value was $210 \text{ mA g}_{\text{Si}}^{-1}$ for cycling tests. Potentiostatic electrochemical impedance spectroscopy (PEIS) was performed with the Gamry EIS unit integrated into the Arbin BT 2000 Battery Tester. The PEIS data were acquired with an amplitude of 10 mV and a frequency range of 15 MHz–1 Hz. Half cells with the same structure but a different Si composite ratio (4:6:1) and weight (5.0 mg) were also applied for galvanostatic intermittent titration technique (GITT) and XPS measurements. The GITT test was performed in the second cycle, during which half cells were (dis)charged for 30 min, rested for 3 hours, and then proceeded to the next (dis)charge step. The *ex situ* XPS test was carried out on Si composites in pristine, discharged, and discharged and charged states. These half cells were tested under a stack pressure of 70 MPa at 60°C .

To prepare Si||NCA full cells, the same two-layer structure SEs were pressed in PEEK tubes. 13.4 mg NCA composite cathode (theoretical areal capacity: 2 mA h cm^{-2} , based on $180 \text{ mA h g}_{\text{NCA}}^{-1}$), and 2.2 mg Si composite anode (mass ratio 6:4:1, theoretical areal capacity: $5.47 \text{ mA h cm}^{-2}$, based on $3579 \text{ mA h g}_{\text{Si}}^{-1}$) were added and pressed at 250 MPa. The areal capacity of NCA is further increased to 3 and 4 mA h cm^{-2} with a fixed NP ratio of 2.74. The cycling performance was tested within a voltage range of 2.4–4.2 V at a current of 0.5C (based on $180 \text{ mA h g}_{\text{NCA}}^{-1}$). These full batteries were also tested under a stack pressure of 70 MPa at 60°C .

Mechanical measurement

The stress change of Si||NCA full cells was evaluated by integrated force sensors with an auxiliary voltage of 0.5–4.5 V, linearly corresponding to 0–103 MPa. The entire structure was rested at 60°C for over 36 h until the stress variation is negligible. The electrochemical tests and auxiliary voltage measurements were initiated simultaneously.

SE powders were pressed into cylinders with a diameter of 10 mm and a height of 1–2 mm. The press pressure is 750 MPa. The cylinders were sealed inside plastic bags and tested by the Instron 4204 machine to obtain compressive stress–strain curves. The compression rate is 0.1 mm min^{-1} .

Author contributions

Y. Huang conducted the experiments, analyzed the data, and wrote the manuscript. Y. Wang assisted in first-principles calculations and analysis. B. Shao assisted in cathode preparation. All authors discussed the results. F. Han conceived the idea and supervised the project.

Conflicts of interest

There are no conflicts to declare.

Acknowledgements

F. Han, Y. Huang, and B. Shao acknowledge the support from US National Science Foundation (Award No. 2223217). F. Han also acknowledges support from the Priti and Mukesh Chatter Career Development Chair Professorship at the Rensselaer Polytechnic Institute.

References

- 1 J. Janek and W. G. Zeier, *Nat. Energy*, 2016, **1**, 1–4.
- 2 C. Ma, Y. Cheng, K. Yin, J. Luo, A. Sharafi, J. Sakamoto, J. Li, K. L. More, N. J. Dudney and M. Chi, *Nano Lett.*, 2016, **16**, 7030–7036.
- 3 S. Wenzel, S. J. Sedlmaier, C. Dietrich, W. G. Zeier and J. Janek, *Solid State Ionics*, 2018, **318**, 102–112.
- 4 Y. Xiao, Y. Wang, S.-H. Bo, J. C. Kim, L. J. Miara and G. Ceder, *Nat. Rev. Mater.*, 2020, **5**, 105–126.
- 5 F. Han, A. S. Westover, J. Yue, X. Fan, F. Wang, M. Chi, D. N. Leonard, N. J. Dudney, H. Wang and C. Wang, *Nat. Energy*, 2019, **4**, 187–196.
- 6 J. Kasemchainan, S. Zekoll, D. Spencer Jolly, Z. Ning, G. O. Hartley, J. Marrow and P. G. Bruce, *Nat. Mater.*, 2019, **18**, 1105–1111.
- 7 T. Krauskopf, F. H. Richter, W. G. Zeier and J. Janek, *Chem. Rev.*, 2020, **120**, 7745–7794.
- 8 K. Takada, *Acta Mater.*, 2013, **61**, 759–770.
- 9 J. Duan, W. Wu, A. M. Nolan, T. Wang, J. Wen, C. Hu, Y. Mo, W. Luo and Y. Huang, *Adv. Mater.*, 2019, **31**, 1807243.
- 10 Y. Huang, B. Shao and F. Han, *J. Mater. Chem. A*, 2022, **10**, 12350–12358.
- 11 S. Cangaz, F. Hippauf, F. S. Reuter, S. Doerfler, T. Abendroth, H. Althues and S. Kaskel, *Adv. Energy Mater.*, 2020, **10**, 2001320.
- 12 T. Inoue and K. Mukai, *ACS Appl. Mater. Interfaces*, 2017, **9**, 1507–1515.
- 13 H. Huo and J. Janek, *ACS Energy Lett.*, 2022, **7**, 4005–4016.
- 14 H. Wu and Y. Cui, *Nano Today*, 2012, **7**, 414–429.
- 15 Y. Jin, B. Zhu, Z. Lu, N. Liu and J. Zhu, *Adv. Energy Mater.*, 2017, **7**, 1700715.
- 16 J. D. McBrayer, M.-T. F. Rodrigues, M. C. Schulze, D. P. Abraham, C. A. Appleby, I. Bloom, G. M. Carroll, A. M. Colclasure, C. Fang, K. L. Harrison, G. Liu, S. D. Minter, N. R. Neale, G. M. Veith, C. S. Johnson, J. T. Vaughey, A. K. Burrell and B. Cunningham, *Nat. Energy*, 2021, **6**, 866–872.
- 17 A. Masias, J. Marcicki and W. A. Paxton, *ACS Energy Lett.*, 2021, **6**, 621–630.
- 18 C.-Y. Wang, T. Liu, X.-G. Yang, S. Ge, N. V. Stanley, E. S. Rountree, Y. Leng and B. D. McCarthy, *Nature*, 2022, **611**, 1–6.
- 19 C. Erk, T. Brezesinski, H. Sommer, R. Schneider and J. Janek, *ACS Appl. Mater. Interfaces*, 2013, **5**, 7299–7307.

- 20 J. Liu, Q. Zhang, T. Zhang, J.-T. Li, L. Huang and S.-G. Sun, *Adv. Funct. Mater.*, 2015, **25**, 3599–3605.
- 21 C. C. Nguyen, T. Yoon, D. M. Seo, P. Guduru and B. L. Lucht, *ACS Appl. Mater. Interfaces*, 2016, **8**, 12211–12220.
- 22 T. Kwon, J. W. Choi and A. Coskun, *Chem. Soc. Rev.*, 2018, **47**, 2145–2164.
- 23 C. Xu, F. Lindgren, B. Philippe, M. Gorgoi, F. Björefors, K. Edstrom and T. Gustafsson, *Chem. Mater.*, 2015, **27**, 2591–2599.
- 24 Z. Xu, J. Yang, H. Li, Y. Nuli and J. Wang, *J. Mater. Chem. A*, 2019, **7**, 9432–9446.
- 25 D. M. Piper, T. A. Yersak and S.-H. Lee, *J. Electrochem. Soc.*, 2012, **160**, A77.
- 26 D. H. Tan, Y.-T. Chen, H. Yang, W. Bao, B. Sreenarayanan, J.-M. Doux, W. Li, B. Lu, S.-Y. Ham, B. Sayahpour, J. Scharf, E. A. Wu, G. Deysher, H. E. Han, H. J. Hah, H. Jeong, J. B. Lee, Z. Chen and Y. S. Meng, *Science*, 2021, **373**, 1494–1499.
- 27 M. Yamamoto, Y. Terauchi, A. Sakuda, A. Kato and M. Takahashi, *J. Power Sources*, 2020, **473**, 228595.
- 28 J. Wu, S. Liu, F. Han, X. Yao and C. Wang, *Adv. Mater.*, 2021, **33**, 2000751.
- 29 A. Sakuda, A. Hayashi and M. Tatsumisago, *Sci. Rep.*, 2013, **3**, 1–5.
- 30 Z. Gu, W. Li, Y. Miao, Y. Chen, X. Xia, G. Chen and H. Liu, *Electrochim. Acta*, 2021, **366**, 137424.
- 31 F. Han, Y. Zhu, X. He, Y. Mo and C. Wang, *Adv. Energy Mater.*, 2016, **6**, 1501590.
- 32 D. Cao, X. Sun, Y. Li, A. Anderson, W. Lu and H. Zhu, *Adv. Mater.*, 2022, 2200401.
- 33 R. Okuno, M. Yamamoto, A. Kato and M. Takahashi, *Electrochem. Commun.*, 2022, **138**, 107288.
- 34 F. Han, J. Yue, X. Zhu and C. Wang, *Adv. Energy Mater.*, 2018, **8**, 1703644.
- 35 S.-J. Choi, S.-H. Choi, A. D. Bui, Y.-J. Lee, S.-M. Lee, H.-C. Shin and Y.-C. Ha, *ACS Appl. Mater. Interfaces*, 2018, **10**, 31404–31412.
- 36 E. Rangasamy, Z. Liu, M. Gobet, K. Pilar, G. Sahu, W. Zhou, H. Wu, S. Greenbaum and C. Liang, *J. Am. Chem. Soc.*, 2015, **137**, 1384–1387.
- 37 S.-J. Choi, S.-H. Lee, Y.-C. Ha, J.-H. Yu, C.-H. Doh, Y. Lee, J.-W. Park, S.-M. Lee and H.-C. Shin, *J. Electrochem. Soc.*, 2018, **165**, A957.
- 38 K. Kisu, S. Kim, H. Oguchi, N. Toyama and S. Orimo, *J. Power Sources*, 2019, **436**, 226821.
- 39 Y. Zhu, X. He and Y. Mo, *ACS Appl. Mater. Interfaces*, 2015, **7**, 23685–23693.
- 40 Y. Yang, Q. Wu, Y. Cui, Y. Chen, S. Shi, R.-Z. Wang and H. Yan, *ACS Appl. Mater. Interfaces*, 2016, **8**, 25229–25242.
- 41 M. N. Obrovac and L. Christensen, *Electrochem. Solid-State Lett.*, 2004, **7**, A93.
- 42 W.-J. Zhang, *J. Power Sources*, 2011, **196**, 877–885.
- 43 M. T. McDowell, S. W. Lee, W. D. Nix and Y. Cui, *Adv. Mater.*, 2013, **25**, 4966–4985.
- 44 K. W. Kim, H. Park, J. G. Lee, J. Kim, Y.-U. Kim, J. H. Ryu, J. J. Kim and S. M. Oh, *Electrochim. Acta*, 2013, **103**, 226–230.
- 45 P. Bärman, B. Krueger, S. Casino, M. Winter, T. Placke and G. Wittstock, *ACS Appl. Mater. Interfaces*, 2020, **12**, 55903–55912.
- 46 W. D. Richards, L. J. Miara, Y. Wang, J. C. Kim and G. Ceder, *Chem. Mater.*, 2016, **28**, 266–273.
- 47 A. Unemoto, T. Ikeshoji, S. Yasaku, M. Matsuo, V. Stavila, T. J. Udovic and S. Orimo, *Chem. Mater.*, 2015, **27**, 5407–5416.
- 48 D. Duveau, S. S. Israel, J. Fullenwarth, F. Cunin and L. Monconduit, *J. Mater. Chem. A*, 2016, **4**, 3228–3232.
- 49 H.-T. Kwon, C. K. Lee, K.-J. Jeon and C.-M. Park, *ACS Nano*, 2016, **10**, 5701–5709.
- 50 R. Reinhold, U. Stoeck, H.-J. Grafe, D. Mikhailova, T. Jaumann, S. Ostwald, S. Kaskel and L. Giebeler, *ACS Appl. Mater. Interfaces*, 2018, **10**, 7096–7106.
- 51 G. L. Coquil, B. Fraisse, N. Dupre and L. Monconduit, *ACS Appl. Energy Mater.*, 2018, **1**, 3778–3789.
- 52 V. Baranchugov, E. Markevich, E. Pollak, G. Salitra and D. Aurbach, *Electrochem. Commun.*, 2007, **9**, 796–800.
- 53 G.-T. Kim, T. Kennedy, M. Brandon, H. Geaney, K. M. Ryan, S. Passerini and G. B. Appetecchi, *ACS Nano*, 2017, **11**, 5933–5943.
- 54 C. Chae, H.-J. Noh, J. K. Lee, B. Scrosati and Y.-K. Sun, *Adv. Funct. Mater.*, 2014, **24**, 3036–3042.
- 55 J. Xiong, J. Yang, G. Wang, T. Saeed, Y. Liu, S. E. Kaczmarek, W. Lu and Q. Wu, *Electrochim. Acta*, 2021, **393**, 139072.
- 56 T. Hatchard and J. R. Dahn, *J. Electrochem. Soc.*, 2004, **151**, A838.
- 57 L. Baggetto, R. A. H. Niessen, F. Roozeboom and P. H. Notten, *Adv. Funct. Mater.*, 2008, **18**, 1057–1066.
- 58 L. Baggetto, J. Oudenhoven, T. van Dongen, J. Klootwijk, M. Mulder, R. Niessen, M. de Croon and P. Notten, *J. Power Sources*, 2009, **189**, 402–410.
- 59 F. Karadas, G. Ertas and S. Suzer, *J. Phys. Chem. B*, 2004, **108**, 1515–1518.
- 60 B. Ulgut and S. Suzer, *J. Phys. Chem. B*, 2003, **107**, 2939–2943.
- 61 T. P. Nguyen and S. Lefrant, *J. Phys.: Condens. Matter*, 1989, **1**, 5197.
- 62 R. Alfonsetti, L. Lozzi, M. Passacantando, P. Picozzi and S. Santucci, *Appl. Surf. Sci.*, 1993, **70**, 222–225.
- 63 R. Koerver, I. Aygün, T. Leichtweiß, C. Dietrich, W. Zhang, J. O. Binder, P. Hartmann, W. G. Zeier and J. Janek, *Chem. Mater.*, 2017, **29**, 5574–5582.
- 64 H. Kuwata, M. Matsui, H. Sonoki, Y. Manabe, N. Imanishi and M. Mizuhata, *J. Electrochem. Soc.*, 2018, **165**, A1486.
- 65 Z. Yu, D. G. Mackanic, W. Michaels, M. Lee, A. Pei, D. Feng, Q. Zhang, Y. Tsao, C. V. Amanchukwu, X. Yan, H. Wang, S. Chen, K. Liu, J. Kang, J. Qin, Y. Cui and Z. Bao, *Joule*, 2019, **3**, 2761–2776.
- 66 F. Lu, Y. Pang, M. Zhu, F. Han, J. Yang, F. Fang, D. Sun, S. Zheng and C. Wang, *Adv. Funct. Mater.*, 2019, **29**, 1809219.
- 67 R. Fantin, E. Trevisanello, R. Ruess, A. Pokle, G. Conforto, F. H. Richter, K. Volz and J. Janek, *Chem. Mater.*, 2021, **33**, 2624–2634.